Nanoscale

PAPER

View Article Online
View Journal | View Issue

Cite this: *Nanoscale*, 2024, **16**, 8639

Tunable abundant valley Hall effect and chiral spin–valley locking in Janus monolayer $VCGeN_4$†

Kang Jia, [a,b] Xiao-Jing Dong, [b] Sheng-Shi Li, [a] Wei-Xiao Ji [a] and Chang-Wen Zhang*[a,b]

It is both conceptually and practically fascinating to explore fundamental research studies and practical applications of two-dimensional systems with the tunable abundant valley Hall effect. In this work, based on first-principles calculations, the tunable abundant valley Hall effect is proved to appear in Janus monolayer $VCGeN_4$. When the magnetization is along the out-of-plane direction, $VCGeN_4$ is an intrinsic ferromagnetic semiconductor with a valley feature. The intriguing spontaneous valley polarization exists in $VCGeN_4$ due to the common influence of broken inversion and time-reversal symmetries, which makes it easier to realize the anomalous valley Hall effect. Furthermore, we observe that the valley-non-equilibrium quantum anomalous Hall effect is driven by external strain, which is located between two half-valley-metal states. When reversing the magnetization, the spin flipping makes the position of the edge state to change from one valley to another valley, demonstrating an intriguing behavior known as chiral spin–valley locking. Although the easy magnetic axis orientation is along the in-plane direction, we can utilize an external magnetic field to transform the magnetic axis orientation. Moreover, it is found that the valley state, electronic and magnetic properties can be well regulated by the electric field. Our works explore the mechanism of the tunable abundant valley Hall effect by applying an external strain and electric field, which provides a perfect platform to investigate the spin, valley, and topology.

Received 7th November 2023,
Accepted 27th March 2024

DOI: 10.1039/d3nr05643k

rsc.li/nanoscale

I. Introduction

Valley (a novel degree of freedom of carriers except spin and charge) and relevant manipulations have become popular topics recently,[1,2] and they feature the appearance of extreme values in energy band structures.[3,4] Good valley systems should possess degenerate and inequivalent valley properties in the inequivalent K points within the momentum space.[5,6] For valley systems, eliminating the degeneracy to realize valley polarization (VP) is regarded as one essential question in valleytronics.[7,8] Some attractive approaches have been put forward to produce VP, such as static magnetic fields,[9,10] magnetic proximity effects,[11,12] optical pumping,[13] and magnetic doping.[14,15] However, there are many challenges in these means. For instance, the valley properties of host systems are usually submerged by the magnetic proximity effect, and clusters are formed in the process of magnetic doping and hence impurity scattering increases. Antiferromagnetic (AFM) materials (for instance, $MnPS_3$ and $MnPSe_3$) have been investigated as valley systems by first-principles calculations.[16] Lately, since spontaneous VP has hopefully come into being, a method of coupling between ferromagnetic (FM) ordering and valleys has been considered,[17–19] stimulating the exploration of the anomalous valley Hall effect (AVHE), and these series of systems are referred to as ferrovalley (FV) materials,[17] which are widely researched. Several two-dimensional (2D) FV materials with in-plane (IP) magnetization have been found in the 2D transition-metal dichalcogenide (TMD) family, comprising CeI_2,[20] ScBrI,[21] ScI_2,[22] and LaBrI[23] monolayers. Nevertheless, the spontaneous VP of FV materials cannot appear for IP magnetization. For the sake of achieving spontaneous VP, it is noteworthy that an external magnetic field can induce the magnetization direction from the IP to out-of-plane (OOP) orientation, which is vital for the exploration of spintronic and valleytronic nanodevices.

In order to find good 2D FV materials with OOP magnetization, many researchers have conducted very fascinating studies. So far, several systems have been explored employing first-principles calculations.[24–28] Many halogen materials have attracted wide attention, such as $RuCl_2$,[25] FeClBr,[26] $OsBr_2$,[27] and $RuBr_2$,[28] because their magnetic and electronic properties can be controlled by substituting different halide atoms. Most notably, through applying strain and varying the electronic cor-

[a]School of Physics and Technology, Institute of Spintronics, University of Jinan, Jinan, Shandong, 250022, People's Republic of China.
E-mail: ss_zhangchw@ujn.edu.cn
[b]School of Physics and Physical Engineering, Qufu Normal University, Qufu, Shandong, 273100, People's Republic of China

†Electronic supplementary information (ESI) available. See DOI: https://doi.org/10.1039/d3nr05643k

relation effect, topological phase transitions can be achieved in RuClBr,[29] $RuCl_2$,[25] OsClBr,[30] $VCSiN_4$,[31] and $RuBr_2$ [28] monolayers. Inspired by many research studies on valleytronics and spintronics,[32–39] the combinations of topological properties and FV states in many materials possibly trigger fresh physics and phenomena.

Recently, one novel 2D system of the MSi_2N_4 (M = Mo, W) family has been experimentally synthesized by the chemical vapor deposition (CVD) method,[40] and researchers found that this method can be utilized to synthesize numerous analogous 2D systems. This materials family possesses lots of intriguing characters, containing topology, VP, transport, and magnetism.[41–49] Ultrathick $MoSi_2N_4(MoN)_4$ has also been recently obtained experimentally[50] and ultrathick $MA_2N_4(M'N)$-intercalated monolayers have also been proposed,[51] which arouse wide public concern. It is discovered that 2D Janus TMD monolayers have been synthesized in experiment.[52] As is known to all, TMD and SiN layers are combined to obtain the MSi_2N_4 family. So, we boldly forecast that the preparation of the Janus MSi_2N_4 family can be realized. For the Janus MSi_2N_4 family, because the middle TMD layer is sandwiched by two diverse layers, the mirror symmetry is broken. The spontaneous OOP dipole has a crucial influence on spin, electronic, valley, and topology properties.

In this work, we found that Janus monolayer $VCGeN_4$ is an intrinsic FM semiconductor with a valley feature, and the interesting tunable abundant valley Hall effect is observed in $VCGeN_4$. Significantly, for OOP magnetization, VP can spontaneously appear on account of breaking of the inversion and time-reversal symmetries, beneficial for exploring the AVHE. Moreover, the valley-nonequilibrium quantum anomalous Hall effect (VQAHE) can be induced between two half-valley-metal (HVM) states by external strain. When reversing the magnetization, the edge state is simultaneously transformed, which indicates that $VCGeN_4$ shows an attractive behavior known as chiral spin–valley locking. Our studies enrich systems with the tunable abundant valley Hall effect and offer a fine candidate in spintronic and valleytronic nanodevices.

II. Computational details

Based on density functional theory (DFT), all calculations were performed in the Vienna *ab initio* simulation package (VASP)[53–55] by employing the projector-augmented-wave (PAW) method. The generalized gradient approximation (GGA) with the Perdew–Burke–Ernzerhof (PBE) functional[56] was utilized to describe the correlation functional. The kinetic energy cutoff, force, and energy convergence criterion were 500 eV, 0.01 eV $Å^{-1}$, and 10^{-6} eV, respectively. Γ-center Monkhorst–Pack grids of 19 × 19 × 1 and 19 × 11 × 1 were adopted for the unit cell and rectangle supercell, respectively. The PBE+U method[57] was applied for the treatment of the 3d orbitals of V atoms and the U value was set to 3.2 eV.[58,59] The band structure from the PBE+U method was compared with that from the Heyd–Scuseria–Ernzerhof (HSE06) hybrid functional.[60] In order to prevent the influences of adjacent layers, a vacuum space of approximate 25 Å was used. The phonon dispersion was acquired using a 3 × 3 × 1 supercell in the PHONOPY code.[61,62] For acquiring the edge state and Berry curvature, the maximally localized Wannier functions were calculated using the WANNIER90 package.[63,64]

III. Results and discussion

It is known that the MSi_2N_4 family has four phases (α, β, γ, and δ phases) by referring to previous research.[65] We build the four phases of $VCGeN_4$ and calculate their energies (see Table S1†). It is found that the α phase is the ground state. In the subsequent discussion, the various properties of the α phase are explored. The crystal structure of $VCGeN_4$ is exhibited in Fig. 1(a) and (b). It shows a hexagonal lattice and the

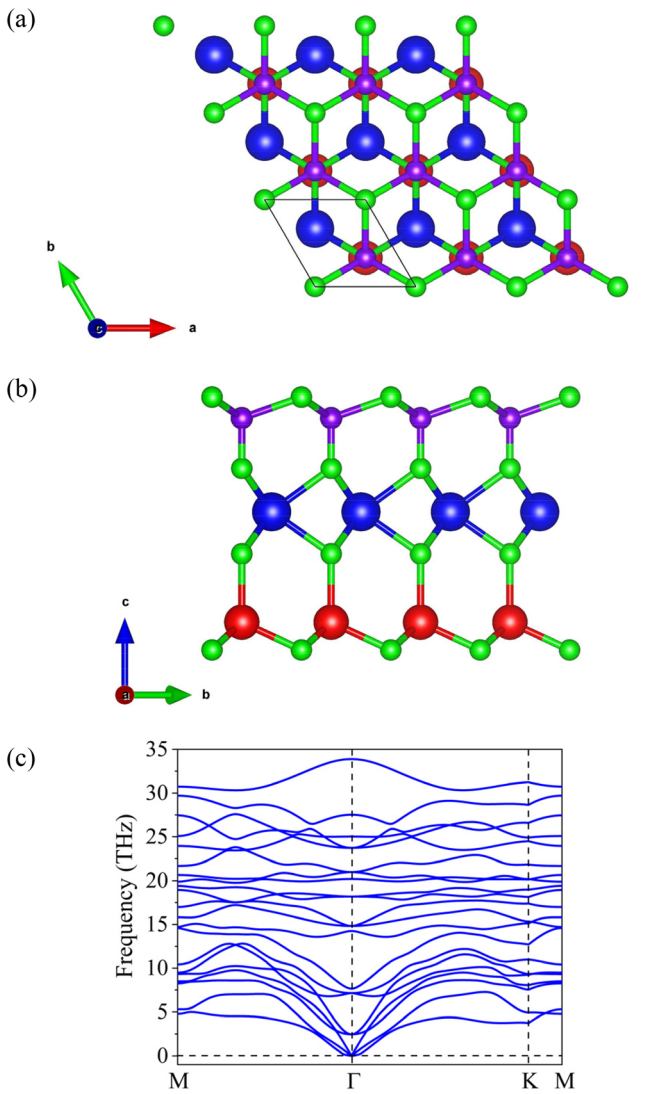

Fig. 1 (a) Top and (b) side views of $VCGeN_4$. The green, purple, blue, and red balls denote N, C, V, and Ge elements, respectively. (c) Phonon dispersion of $VCGeN_4$.

space group of $P3m1$ (no. 156). Each unit cell includes four N atoms, one C atom, one V atom, and one Ge atom, which are stacked with seven atomic layers in the order of N–C–N–V–N–Ge–N. Each inner V atom is surrounded by six neighboring N atoms, constituting a trigonal prismatic structure, and this VN_2 layer is sandwiched by C–N and Ge–N bilayers. $VCGeN_4$ can be obtained by changing the Ge (C) atom of one of the two GeN (CN) bilayers in monolayer VGe_2N_4 (VC_2N_4) with the C (Ge) atom. The lattice constant of $VCGeN_4$ is optimized to 2.85 Å. The phonon dispersion is investigated. As is displayed in Fig. 1(c), all branches are positive in the entire Brillouin zone (BZ), confirming that the $VCGeN_4$ is dynamically stable.

To research the stability of $VCGeN_4$, the cohesive energy is first calculated, which is defined as $E_{coh} = (E_V + E_C + E_{Ge} + 4E_N - E_{VCGeN_4})/7$. Here, E_V, E_C, E_{Ge}, and E_N are the total energies of the isolated V, C, Ge, and N atoms, while E_{VCGeN_4} is the total energy of the $VCGeN_4$ unit cell. The obtained E_{coh} is 4.08 eV per unit cell. The relative large and positive value is comparable to those of theoretical and experimental 2D materials, such as CeI_2 (3.14 eV per unit cell),[20] phosphorene (3.48 eV per unit cell),[66] and Cu_2Ge (3.17 eV per unit cell),[67] indicating that it is possible to synthesize $VCGeN_4$ in the laboratory. The formation energy is also obtained from $E_{form} = (\mu_V + \mu_C + \mu_{Ge} + 4\mu_N - E_{VCGeN_4})/7$, where μ_V, μ_C, μ_{Ge}, and μ_N are the energies of per V, C, Ge, and N atom in the related stable bulk phases, respectively. The E_{form} is 2.62 eV per unit cell, which implies that the synthesis of $VCGeN_4$ is an exothermic reaction.

Then, we perform *Ab initio* molecular dynamics (AIMD) simulations to evaluate the thermal stability of $VCGeN_4$ at room temperature. As shown in Fig. S1,† the total energy fluctuates around the equilibrium values and no destruction is found in the final configuration, which suggests good thermal stability. Moreover, the mechanical properties of $VCGeN_4$ are investigated. Because of the hexagonal symmetry, $VCGeN_4$ has two independent elastic constants (C_{12} and C_{11}), and the acquired C_{12} and C_{11} values are 142.08 Nm^{-1} and 226.54 Nm^{-1}, respectively. The C_{ij} values of $VCGeN_4$ meet the Born criteria ($C_{11} > 0$ and $C_{11}–C_{12} > 0$),[68–70] confirming the mechanical stability. In short, all these calculations jointly demonstrate that $VCGeN_4$ has excellent structural stability.

The magnetic properties of $VCGeN_4$ are discussed. Our calculation results illustrate that $VCGeN_4$ stabilizes into the FM configuration, and the AFM state is 153 meV higher in energy than its FM state using a rectangle supercell (see Fig. S2†). For $VCGeN_4$, the bonding angle of V–N–V is 88.7°, close to 90°. In accordance with the Goodenough–Kanamori–Anderson rules,[71–73] such a structural trait prefers the FM state, consistent with our conclusions. The stable FM coupling is prohibited for the 2D isotropic Heisenberg model, on account of the Mermin–Wagner theorem.[74] Nevertheless, the long-range magnetic order is protected by finite magnetic anisotropy. Hence, the stability of FM configuration in $VCGeN_4$ is strongly related to its MAE, which mainly includes the magnetocrystalline anisotropy (MCA) energy E_{MCA} and the magnetic shape anisotropy (MSA) energy E_{MSA}. The E_{MCA} and E_{MSA} are induced by the SOC effect and the dipole–dipole (D–D) interaction, respectively. The D–D interaction can be written as

$$E_{D-D} = -\frac{1}{2}\frac{\mu_0}{4\pi}\sum_{i\neq j}\frac{1}{r_{ij}^3}\left[\vec{M}_i\cdot\vec{M}_j - \frac{3}{{r_{ij}}^2}\left(\vec{M}_i\cdot\vec{r}_{ij}\right)\left(\vec{M}_j\cdot\vec{r}_{ij}\right)\right] \quad (1)$$

where $\vec{M}_i$ $(\vec{M}_j)$ is the local magnetic moment and $\vec{r}_{ij}$ represents vectors which connect sites j and i. The E_{MCA} is defined as the energy discrepancy between the IP and OOP magnetizations: $E_{MCA} = E_{x/y} - E_z$. The calculated E_{MCA} of $VCGeN_4$ is −48 μeV. The E_{MSA} is obtained by the energy discrepancy with the magnetization orientation rotating from the IP direction to the OOP direction. The calculated E_{MSA} is −28 μeV, hence the MAE of $VCGeN_4$ is −76 μeV. The negative (positive) MAE represents that the easy magnetic axis is parallel (perpendicular) to the plane. The calculated MAE (−76 μeV) means that the easy magnetic axis direction is along the IP, which indicates that there is no energy barrier for the rotation of the magnetic axis in the xy plane.[20] Therefore, $VCGeN_4$ is regarded as a 2D *XY* magnet.[20] For 2D *XY* magnets with typical triangle lattice structures, the Berezinskii–Kosterlitz–Thouless (BKT) magnetic transition has been determined at a crucial temperature T_C. Monte Carlo simulations are utilized to estimate the crucial temperature $T_C = 1.335J/k_B$, where k_B and J are the Boltzmann constant and the nearest-neighbor (NN) exchange parameter, respectively. The J is determined by the energy difference between the AFM state energy E_{AFM} and FM state energy E_{FM}. According to the AFM and FM configurations, the corresponding energies of AFM and FM states can be acquired from the following equations:

$$E_{FM} = E_0 - (6J + 2A)S^2 \quad (2)$$

$$E_{AFM} = E_0 + (2J - 2A)S^2 \quad (3)$$

where E_0 and A are the total energy of the system and anisotropy parameter, respectively. The J can be calculated by

$$J = (E_{AFM} - E_{FM})/8S^2 \quad (4)$$

The obtained J is 19.13 meV when $S = 1$ and the T_C is calculated to be 296 K.

The electronic and topological states of 2D materials are influenced by the magnetic anisotropy.[25–30,75] It is widely known that the magnetization belongs to pseudovectors. For the OOP FM system, the horizontal mirror symmetry of the system can be maintained, but all vertical mirrors are broken. The maintained horizontal mirror symmetry permits a non-vanishing Chern number and spontaneous VP.[75] Although the easy magnetic axis orientation of $VCGeN_4$ is along the IP, we can apply an external magnetic field to transform the magnetic axis orientation, which brings new ideas to our research. The effect of different electronic correlations (U values) on the electronic properties of the $VCGeN_4$ is explored to acquire the accurate electronic structures. As shown in Fig. S3,† for 0.0 eV ≤ U ≤ 2.0 eV and 2.5 eV ≤ U ≤ 4.0 eV, $VCGeN_4$ exhibits indirect and direct band-gap semiconductor features, respectively. In particular, when the U value increases to 3.2 eV (see Fig. 2(b)),

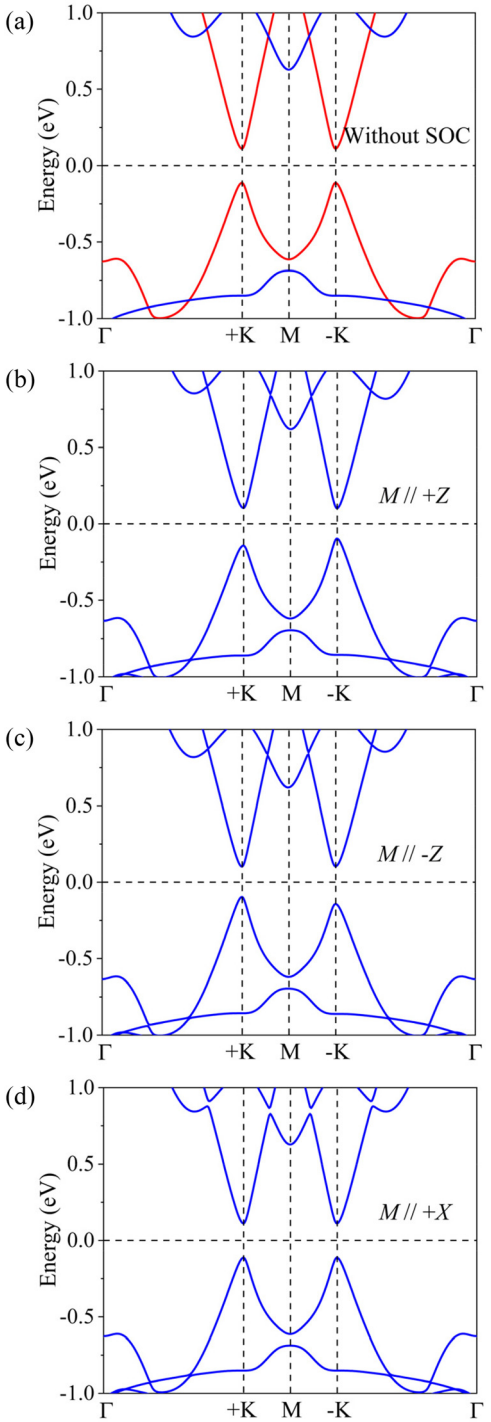

Fig. 2 The band structures of $VCGeN_4$ (a) without SOC and with SOC for the magnetization of V along the (b) positive *Z*, (c) negative *Z*, and (d) positive *X* directions, respectively. For (a), the red (blue) lines denote the spin-up (spin-down) direction.

the band structure is very consistent with that obtained using the HSE06 functional (see Fig. S4†). It is seen that the band gap of 0.95 eV obtained using the HSE06 functional is larger than that obtained by the PBE+*U* method. The U = 3.2 eV is chosen to discuss the valley and topology in the following exploration.

The spin-polarized energy band structures of $VCGeN_4$ are plotted in Fig. 2. Because of the exchange interaction, Fig. 2(a) exhibits an evident spin splitting, and $VCGeN_4$ is a narrow direct-band-gap semiconductor with a band-gap value of 0.22 eV. The conduction band minimum (CBM) and valence band maximum (VBM) are located at the −K and +K points, which are offered by the spin-up channels. For both the valence band (VB) and the conduction band (CB), the energies of the +K and −K valleys are degenerate. Some materials have valleys only in the CB or VB. Notably, degenerate valleys are formed in both the CB and VB, indicating that $VCGeN_4$ is a potential valleytronic semiconductor. The d orbitals of V atoms lie in the trigonal prismatic crystal fields and the d orbitals can split into d_{xz} + d_{yz}, d_{xy} + $d_{x^2-y^2}$ and low-lying d_{z^2} orbitals. According to the orbital-projected band structure (see Fig. 3), for the spin-up channels, the only one electron occupies the d_{z^2}-controlled top VB. It is expected that each V atom has the magnetic moment of $1\mu_B$, which accords with our calculated value of $1.2\mu_B$.

When involving the SOC and OOP magnetic anisotropy, as shown in Fig. 2(b), we find that the VP is induced. For the top VB, the energy in the +K valley is smaller than that of the −K valley and the spontaneous VP is 46 meV, while the VP of the bottom CB is 2 meV. When the magnetization of V is reversed, as shown in Fig. 2(c), the VPs of both the VB and CB are flipped and the valleys are contributed by the spin-down channels. Fig. 2(b) and (c) indicate that $VCGeN_4$ is still a direct-band-gap semiconductor and the band-gap value is 0.20 eV. According to Fig. 2(d), the VP cannot be found with IP magnetic anisotropy.

The underlying physics of spontaneous VP in $VCGeN_4$ can be comprehended to the combined influence of magnetic exchange interaction and SOC. When involving magnetic exchange interaction but excluding SOC, because of the broken time-reversal symmetry, the spin splitting of energy band structures in the −K and +K valleys is $\Delta_{mag}^{-K} = \Delta_{mag}^{+K}$ ($\Delta^{-K(+K)} = E_{\uparrow}^{-K(+K)} - E_{\downarrow}^{-K(+K)}$, where ↓ and ↑ represent spin-down and spin-up channels, respectively.) Moreover, when

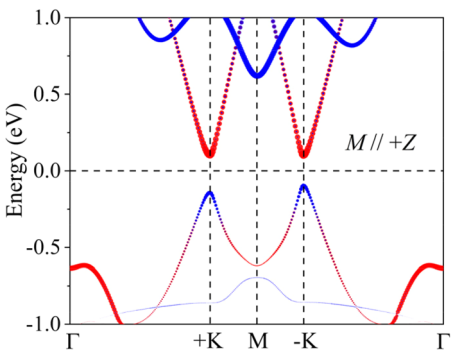

Fig. 3 The orbital-projected band structure of $VCGeN_4$ when the magnetization is along the positive *Z* direction. The red and blue symbols denote the d_{z^2} and $d_{x^2-y^2}/d_{xy}$ orbital components of V, respectively.

excluding magnetic exchange interaction but considering SOC, the spin splitting also appears in the −K and +K valleys. However, due to the inversion symmetry breaking and time-reversal symmetry protecting, the signs of the valley splitting in the −K and +K valleys are opposite, but the absolute values are the same, namely $\Delta_{SOC}^{-K} = -\Delta_{SOC}^{+K}$. Hence, when taking into account both magnetic exchange interaction and SOC, the spin splitting is $\Delta_{mag}^{-K} + \Delta_{SOC}^{-K}$ in the −K valley and $\Delta_{mag}^{+K} + \Delta_{SOC}^{+K}$ in the +K valley, respectively, resulting in the interesting spontaneous VP.

As described above, for $VCGeN_4$, the VP of the VB is 46 meV, nevertheless, that in the CB is inconspicuous. The difference is relevant to the situation that valleys in the VB and CB are dominated by different orbitals. As shown in Fig. 3, it can be found that the −K and +K valleys in the CB are contributed by V-d_{z^2} orbitals, while the −K and +K valleys in the VB are mainly dominated by $d_{xy} + d_{x^2-y^2}$ orbitals. We calculate the total and partial density of states (DOS) of $VCGeN_4$. As shown in Fig. S5,† the bottom CB primarily consists of d_{z^2} orbitals of V and the top VB is mainly composed of $d_{xy} + d_{x^2-y^2}$ orbitals of V and minority p_z orbitals of N, which is in agreement with the orbital-resolved band structure (see Fig. 3). Because of the significant role of SOC in the VP, in order to obtain the underlying physics, a simple model is employed:

$$\hat{H}_{SOC} = \lambda \hat{L} \cdot \hat{S} = \hat{H}_{SOC}^{0} + \hat{H}_{SOC}^{1} \tag{5}$$

where $\hat{L}$ is the orbital angular momentum and $\hat{S}$ is the spin angular momentum. $\hat{H}_{SOC}^{1}$ and $\hat{H}_{SOC}^{0}$ represent the interactions between opposite spin states and between the same spin states, respectively. It can be seen that the −K and +K valleys in the CB and VB only consist of the spin-up channel, while the spin-down channel lies far away from the −K and +K valleys. Hence, $\hat{H}_{SOC}^{1}$ can be ignored here. Considering $\hat{H}_{SOC}^{0}$, it can be shown by the polar angles θ and ϕ:

$$\begin{aligned}\hat{H}_{SOC} &\approx \hat{H}_{SOC}^{0} \\ &= \lambda \hat{S}_{Z'} \left(\hat{L}_Z \cos\theta + \frac{1}{2}\hat{L}_+ e^{-i\varphi} \sin\theta + \frac{1}{2}\hat{L}_- e^{+i\varphi} \sin\theta \right)\end{aligned} \tag{6}$$

For the OOP magnetization orientation (θ = 0°), the $\hat{H}_{SOC}$ can be written as

$$\hat{H}_{SOC}^{0} = \lambda \hat{S}_Z \cdot \hat{L}_Z = \alpha \hat{L}_Z \tag{7}$$

Because the symmetry of $VCGeN_4$ is C_{3v}, we chose the following basis functions

$$|\varphi_v^{\tau}\rangle = \sqrt{\frac{1}{2}}\left(|d_{x^2-y^2}\rangle + i\tau|d_{xy}\rangle\right) \tag{8}$$

$$|\varphi_c^{\tau}\rangle = |d_{z^2}\rangle \tag{9}$$

where τ, c, and v indicate the valley index, CB, and VB, respectively. The energy levels of valleys in the CB and VB are

$$E_c^{\tau} = \langle \varphi_c^{\tau} | \hat{H}_{SOC}^{0} | \varphi_c^{\tau} \rangle \tag{10}$$

$$E_v^{\tau} = \langle \varphi_v^{\tau} | \hat{H}_{SOC}^{0} | \varphi_v^{\tau} \rangle \tag{11}$$

Consequently, the VP between valleys is given by

$$\begin{aligned}\Delta E_v = E_v^{-K} - E_v^{+K} &= i\langle d_{xy}|\hat{H}_{SOC}|d_{x^2-y^2}\rangle \\ &- i\langle d_{x^2-y^2}|\hat{H}_{SOC}|d_{xy}\rangle = 4\alpha\end{aligned} \tag{12}$$

$$\Delta E_c = E_c^{-K} - E_c^{+K} = 0 \tag{13}$$

In accordance with these discussions, the discrepancy of the VP can be clearly comprehended. In particular, if the magnetization orientation is not taken into account, the VP of the VB can be written as $\Delta E_v = 4\alpha \cos\theta$ (θ = 90° and 0° represent IP and OOP orientations, respectively), which explains that the VP cannot be observed for the IP orientation (see Fig. 2(d)).

After verifying the spontaneous VP of $VCGeN_4$, then the Berry curvature $\Omega(k)$ is investigated to evaluate its electronic transport features, which is obtained by utilizing the following Kudo formula:[76]

$$\Omega(k) = -\sum_n \sum_{n \neq n'} f_n \frac{2\mathrm{Im}\langle \psi_{nk}|v_x|\psi_{n'k}\rangle\langle \psi_{n'k}|v_y|\psi_{nk}\rangle}{(E_n - E_{n'})^2} \tag{14}$$

where f_n, $\langle \psi_{nk}|$, and v_x (v_y) are the Fermi–Dirac distribution function, the Bloch wave function related to the eigenvalue E_n, and velocity operators, respectively. Fig. 4(a) and (b) display the calculated $\Omega(k)$ of $VCGeN_4$ over the 2D BZ and along the high-symmetry path. It is obvious that in the vicinity of the −K and +K valleys, the signs of $\Omega(k)$ is opposite and the absolute

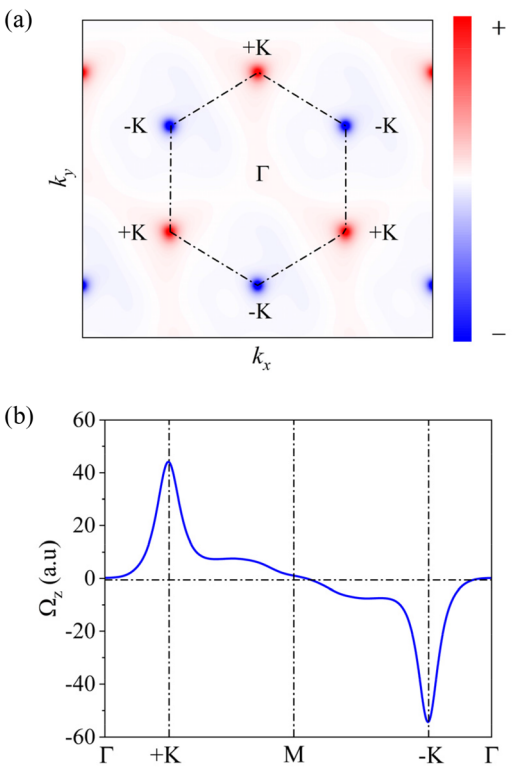

Fig. 4 The Berry curvatures of $VCGeN_4$ (a) in the BZ and (b) along the high-symmetry points.

values are not identical, illustrating the valley-contrasting feature of $VCGeN_4$. Consequently, for p-type $VCGeN_4$, when the longitudinal electric field is used, the holes can acquire opposite transverse anomalous velocities in the −K and +K valleys, because $\upsilon \propto E \times \Omega$. So, the spin-polarized AVHE can be expected (see Fig. 4(a)). In addition, the absolute value of $\Omega(k)$ for the +K valley is smaller than that for the −K valley, and the accumulation of net charge is observed (see Fig. 5(a)). It must be stressed that the flip of spin polarization and valley cause the absolute value of $\Omega(k)$ for the −K and +K valleys to exchange; nevertheless, the signs of $\Omega(k)$ are not varied. Moreover, the flipping of the magnetization can give rise to the sign variation of the driven voltage, but its magnitude remains unchanged (see Fig. 5(b)). Besides this, the FV properties are widely applied in multiple functional nanodevices. Recently, Feng *et al.* proposed a novel concept of contact-limited valley-contrasting current injection,[77] which can generate gate-tunable valley-polarized injection current. It provides a new idea for VP manipulation.

It is well known that epitaxial strain is an effective tool in the manipulation of the topological, magnetic, and electronic properties of 2D systems. Here, biaxial strain is introduced into $VCGeN_4$. The strain is defined as $\varepsilon = (a - a_0)/a_0$, where a (a_0) is the strained (unstrained) lattice constant. In our work, we take into account a rational strain range of $-5\% \le \varepsilon \le 5\%$. The positive (negative) ε value refers to the tensile (compressive) strain. We utilize a rectangle supercell to compare the energy discrepancy between different magnetic configurations (AFM and FM) under strain. According to Fig. S6,† the FM ground state is very stable in the investigated strain range. The band structures of some representative ε values without SOC are exhibited in Fig. S7.† When $-5\% \le \varepsilon \le -3\%$ and $4\% \le \varepsilon \le 5\%$, $VCGeN_4$ is an indirect-gap semiconductor. For $-2\% \le \varepsilon \le 3\%$, $VCGeN_4$ has the direct-gap semiconductor character, so this strain range will be emphatically explored in the following research. Both the +K and −K valleys in the CB and VB are occupied by the spin-up states.

Because the symmetry of 2D systems can be affected by the direction of magnetic anisotropy, which can have important impact on the electronic and topological states. First, we assume that the magnetocrystalline direction of $VCGeN_4$ is along the OOP for the considered strain range. The band structures of some representative ε values are shown in Fig. S8† and the global band-gap *versus* strain is displayed in Fig. 6. The consequences indicate that the band-gap obviously varies in

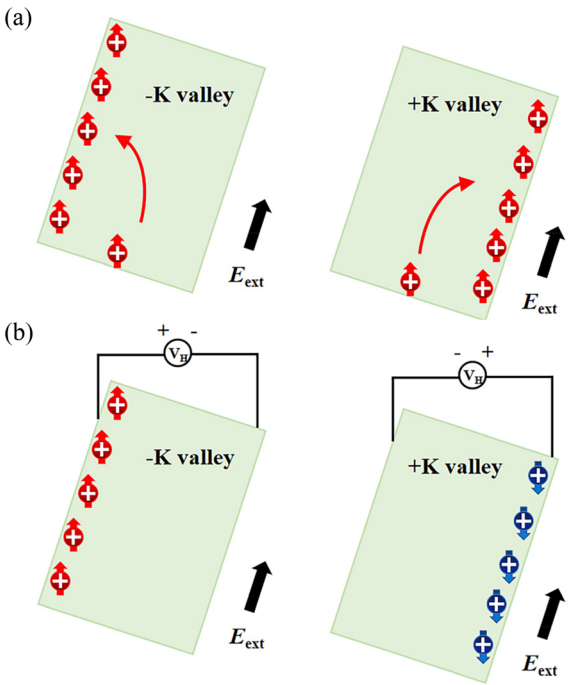

Fig. 5 (a) Schematics of the AVHE in the −K and +K valleys for hole-doped $VCGeN_4$ when the magnetization is along the +Z direction. (b) Schematics of the Hall voltages for hole-doped $VCGeN_4$ when the magnetization is along the +Z (left) and −Z (right) directions, respectively. The red and blue balls denote spin-up and spin-down carriers, respectively.

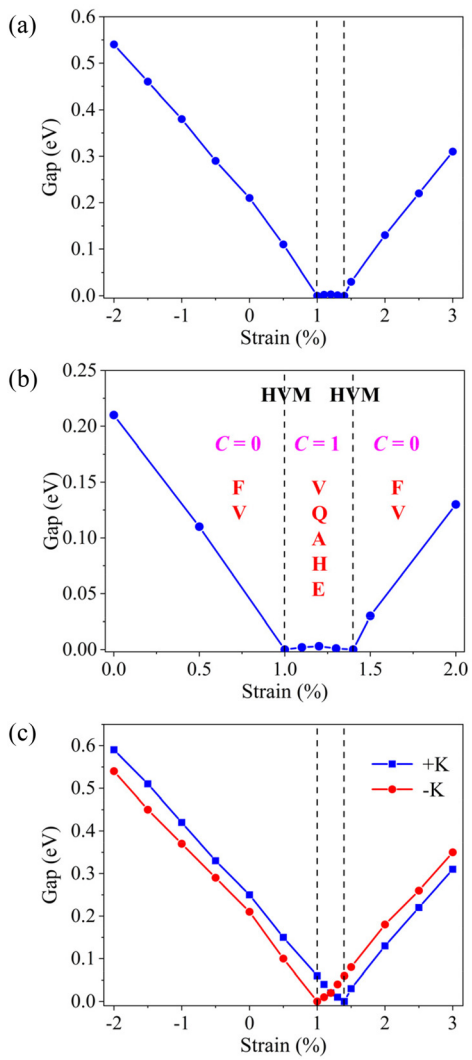

Fig. 6 (a) The global band gaps with OOP magnetization as a function of strain and (b) phase diagram exhibited with different strains. (c) Band gaps in the +K and −K valleys as a function of strain.

various strains. In particular, when ε = 1% or 1.4%, the system turns into the HVM state, where two valleys are semiconductor and metallic, respectively, and has 100% VP, which is similar to the semi-metallic behaviour with 100% spin polarization in spintronics. Because the SOC is always involved in the calculations, the perfect 100% spin polarization can be obtained in the HVM state with the identical spin channel. For traditional semi-metals, it is notable that spin-down and spin-up states are usually mixed because of the SOC. For $-2\% \leq \varepsilon \leq 1\%$, the global band-gap gradually decreases with increasing strains and the HVM state vanishes, while the VP remains in the VB. In particular, when $1.4\% \leq \varepsilon \leq 3\%$, the VP remains in the CB, and as the strain increases, the global band-gap increases. We can observe some little band gaps between ε = 1% and 1.4%.

As previously mentioned, the diverse VP behavior can be attributed to the contribution in the +K and −K valleys of the CB and VB from diverse orbital components. In all strain regions, the d_{xy} + $d_{x^2-y^2}$ or d_{z^2} orbitals of V atoms primarily occupy the +K and −K valleys in the CB and VB. The orbital-resolved band structures of ε = 0.5%, 1.2%, and 2% are shown in Fig. S9.† When $1.4\% < \varepsilon < 5\%$, the d_{z^2} orbitals occupy the +K and −K valleys of the VB, but the two valleys of the CB are from d_{xy} + $d_{x^2-y^2}$ orbitals (such as ε = 2%). For $1\% < \varepsilon < 1.4\%$, the orbital features in the −K valley are not varied, and the d_{xy} + $d_{x^2-y^2}$ (d_{z^2}) orbitals occupy the +K valleys in the VB (CB) (such as ε = 1.2%). When $-5\% < \varepsilon < 1\%$, we can acquire the opposite distributions (such as ε = 0.5%) in contrast to the situations of $1.4\% < \varepsilon < 5\%$.

As the ε changes, the two-time inversions of orbital compositions can be observed together with the emergence of two HVM states, which indicates that topological phase transition may occur. The ε = 1.2% is chosen as an instance to prove our consideration. As plotted in Fig. 7(a), a nontrivial chiral edge state connects the VB and CB, demonstrating that $VCGeN_4$ features a VQAHE and has a unit Chern number (C). On account of the VBM and CBM being contributed by spin-up channels, the chiral edge state has 100% spin polarization and spin-up character. While the magnetization orientation of V is flipped, the chiral edge state can be transformed correspondingly, which is analogous to the flipping of VP. According to Fig. 7(b), the edge state with spin-down channels and opposite chirality can cross the bulk band gap and connect the CB and the VB. In addition, the spin flipping makes the position of edge state to shift from one valley to another valley, indicating a pattern known as chiral spin–valley locking.

Because the variations of electronic states are closely connected with the transition of $\Omega(k)$, the $\Omega(k)$ distributions for ε = 0.5%, 1.2%, and 2% are plotted in Fig. S10.† According to Fig. S10(a) and (d),† for ε = 0.5%, $\Omega(k)$ has opposite signs with unequal absolute values in the +K and −K valleys for FV states, demonstrating the classic valley-contrasting traits. Under ε = 1.2%, both the absolute value and sign of $\Omega(k)$ in the −K valley are changed (see Fig. S10(b) and (e)†) on account of the appearance of topological phase transition. That is to say, the magnitudes of $\Omega(k)$ are inconsistent and the signs are consistent in the two valleys for $1\% < \varepsilon < 1.4\%$. Such a situation of $\Omega(k)$ can bring about non-zero C and non-trivial topological properties. C = 1 can be obtained by $C = \frac{1}{2\pi}\int_{BZ} d^2k\Omega(k)$, which is analogous to the nontrivial chiral edge states (see Fig. 7(a) and (b)). When $\varepsilon > 1.4\%$, the VQAHE state transforms into the FV state, leading to the sign variation of $\Omega(k)$ in the +K valley (for instance, under ε = 2%, see

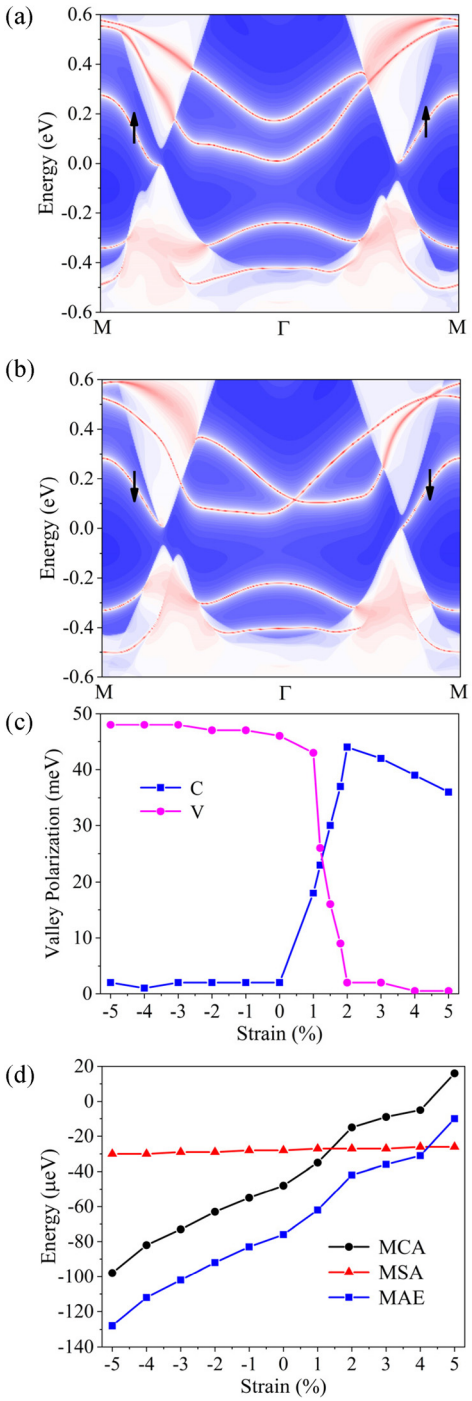

Fig. 7 Edge states under ε = 1.2% along (a) the positive Z direction and (b) the negative Z direction, respectively, for $VCGeN_4$ with OOP magnetization. (c) VP in both the VB (V) and CB (C) as a function of strain. (d) Calculated MCA energy, MSA energy, and MAE as a function of strain.

Fig. S10(c) and S10(f)†). All in all, we can observe the sign-reversal $\Omega(k)$ in two valleys with increasing strain.

Tellingly, $VCGeN_4$ can realize spontaneous VP when the magnetization direction is along the OOP, and the VP in the top VB and bottom CB is observed (see Fig. S8† and Fig. 7(c)). When $1.4\% < \varepsilon < 5\%$, a noticeable VP can be observed in the bottom CB, but these in the top VB is almost be ignored. Nevertheless, compared with the circumstance of $1.4\% < \varepsilon < 5\%$, the distribution of the VP for $-5\% < \varepsilon < 1\%$ is opposite. We can account for these consequences utilizing the distribution of different orbitals (d_{xy} + $d_{x^2-y^2}$ and d_{z^2} orbitals of V atoms). For $1\% < \varepsilon < 1.4\%$, the VP can be discovered in the VB and CB, and $VCGeN_4$ features a VQAHE in this region.

The situations of the magnetocrystalline direction along IP are explored. Some representative electronic structures are displayed in Fig. S11† and the band gaps *versus* strain are shown in Fig. S12.† When $-2\% \leq \varepsilon \leq 3\%$, with increasing strain, the band gap initially decreases and drops to 0, afterwards reopens and goes up. The band gap is closed in approximate $\varepsilon = 1.2\%$, and we cannot observe spontaneous VP and the VQAHE state. For $-2.5\% \leq \varepsilon \leq 3.25\%$ (except $\varepsilon = 1.2\%$), $VCGeN_4$ is a direct-band-gap semiconductor. When $-5\% < \varepsilon < -2.5\%$ and $3.25\% < \varepsilon < 5\%$, $VCGeN_4$ is an indirect-band-gap semiconductor. For $\varepsilon = 1.2\%$, $VCGeN_4$ has a semi-metal character. In brief, $VCGeN_4$ is a conventional semi-metal or FM semiconductor.

Then, the influence of strain on MAE is discussed. The MCA energy, MSA energy, and MAE *vs.* strain are plotted in Fig. 7(d). According to Fig. 7(d), for $-5\% \leq \varepsilon \leq 5\%$, the variation of MSA energy (-30 μeV $< E_{MSA} < -26$ μeV) is relatively stable and the negative MAE can be found all the time, manifesting that the magnetocrystalline direction of $VCGeN_4$ is always along the IP in the investigated strain range. Nevertheless, we can adjust the magnetization from the IP to OOP *via* making use of an external magnetic field to overcome the energy barrier, which will come into being intriguing electronic and topological states. For instance, when $\varepsilon = 1.2\%$, the energy barrier of around 58 μeV corresponds to the application of an external magnetic field of about 0.29–0.58 T. Moreover, in order to comprehend the underlying physics of different MAEs, the atom-projected MCA energy without strain is obtained (see Fig. 8(a)). It is discovered that the IP MCA energy is mainly contributed by the p and d orbitals of the V atom (see Fig. 8(b) and (c)). The summations of orbital interaction lead to the MCA energy, and the p and d orbitals of V in $VCGeN_4$ offer values of -6.74 μeV per f.u. and -38.62 μeV per f.u., respectively.

The electric field is always applied to tune the electronic and magnetic features.[78,79] Therefore, we explore the influence of the electric field with a magnitude of 0.1–0.6 V Å^{-1}. The magnetic interactions are discussed under the electric field. It is found that $VCGeN_4$ maintains the FM state within an investigated electric field range (see Fig. S13†), and the increasing electric field can enhance the FM coupling. Fig. S14(a)† shows the obtained results of MCA energy, MSA energy, and MAE with the electric field. It is discovered that the MCA energy, MSA energy, and MAE of $VCGeN_4$ are always negative, which

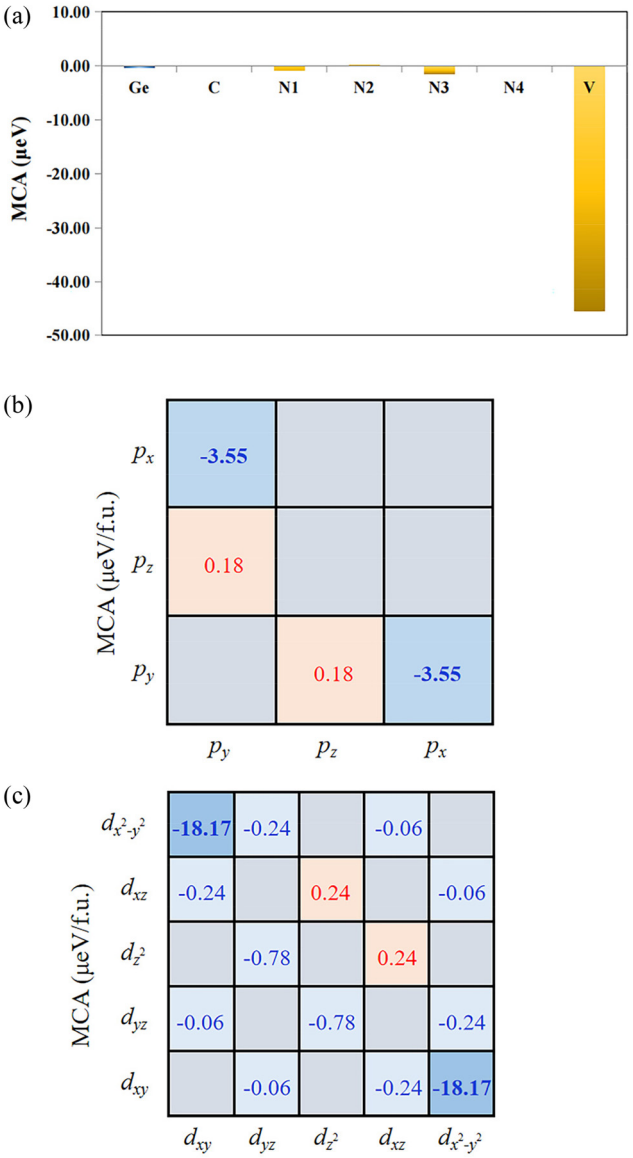

Fig. 8 (a) Atom-resolved MCA energy and orbital-resolved MCA energies of (b) V-p and (c) V-d for $VCGeN_4$.

shows that the easy magnetic axis direction is always along the IP. According to Fig. S14(b),† due to the enhancement of FM coupling with the electric field from 0.1 V Å^{-1} to 0.6 V Å^{-1}, the T_C monotonically increases.

The electronic structures of $VCGeN_4$ under an electric field E are investigated. For OOP magnetization, the variations of the global band gap, the VP for the VB and CB *versus* E, and the band structures at the representative E are shown in Fig. S14(c), S14(d), and S15,† respectively. It is found that $VCGeN_4$ is intrinsically a FV system for E between 0.1 V Å^{-1} and 0.6 V Å^{-1}. The band gap increases with increasing E (when 0.1 V Å^{-1} $\leq E \leq$ 0.6 V Å^{-1}). As shown in Fig. S14(d) and S15,† within the discussed E section, the VP of the VB is noteworthy, but the VP of the CB is inconspicuous, which can be understood by the situation of V-d orbitals. Fig. S16† presents the

$\Omega(k)$ of $VCGeN_4$ under E = 0.1 V Å^{-1} with SOC. It is found that the $\Omega(k)$ dominantly emerges in the +K and −K valleys with unequal absolute values and opposite signs. Our works demonstrate that many characteristics of 2D materials can well regulated by the electric field, such as the valley state and electronic and magnetic properties.

IV. Conclusion

In summary, *via* first-principles calculations, the tunable abundant valley Hall effect is reported in $VCGeN_4$. $VCGeN_4$ is an intrinsic ferromagnetic semiconductor and has a valley feature. For OOP magnetization, arising from the breaking of inversion and time-reversal symmetries, the VP can spontaneously occur, motivating the exploration of charge, spin, and the AVHE. In addition, under tensile strain, band inversion can be realized in the +K and −K valleys, which induces the VQAHE. In particular, the valley feature can be maintained with an external strain and electric field, manifesting that the tunable abundant valley Hall effect exists in $VCGeN_4$. All discoveries greatly enrich the tunable abundant valley Hall effect and point out a promising material for investigating the tunable abundant valley Hall effect in experiment.

Conflicts of interest

There are no conflicts of interest to declare.

Acknowledgements

This work was supported by the National Natural Science Foundation of China (grant no. 52173283), the Taishan Scholar Program of Shandong Province (grant no. ts20190939), and the Independent Cultivation Program of Innovation Team of Jinan City (grant no. 2021GXRC043).

References

1 K. F. Mak, D. Xiao and J. Shan, Light-valley interactions in 2D semiconductors, *Nat. Photonics*, 2018, **12**, 451–460.
2 D. Xiao, G. B. Liu, W. Feng, X. Xu and W. Yao, Coupled spin and valley physics in monolayers of MoS_2 and other group VI dichalcogenides, *Phys. Rev. Lett.*, 2012, **108**, 196802.
3 K. F. Mak, K. L. McGill, J. Park and P. L. McEuen, The valley Hall effect in MoS_2 transistors, *Science*, 2014, **344**, 1489–1492.
4 S. Wu, J. Ross, G. B. Liu, G. Aivazian, A. Jones, Z. Y. Fei, W. G. Zhu, D. Xiao, W. Yao, D. Cobden and X. D. Xu, Electrical tuning of valley magnetic moment through symmetry control in bilayer MoS_2, *Nat. Phys.*, 2013, **9**, 149–153.
5 J. R. Schaibley, H. Y. Yu, G. Clark, P. Rivera, J. S. Ross, K. L. Seyler, W. Yao and X. D. Xu, Valleytronics in 2D materials, *Nat. Rev. Mater.*, 2016, **1**, 16055.
6 S. A. Vitale, D. Nezich, J. O. Varghese, P. Kim, N. Gedik, P. Jarillo-Herrero, D. Xiao and M. Rothschild, Valleytronics: opportunities, challenges, and paths forward, *Small*, 2018, **14**, 1801483.
7 Q. Y. Zhang, S. Yang, W. B. Mi, Y. C. Cheng and U. Schwingenschlogl, Large spin-valley polarization in monolayer $MoTe_2$ on top of EuO (111), *Adv. Mater.*, 2016, **28**, 959–966.
8 G. Pacchioni, Valleytronics with a twist, *Nat. Rev. Mater.*, 2020, **5**, 480.
9 G. Aivazian, Z. R. Gong, A. Jones, R. L. Chu, J. Yan, D. G. Mandrus, C. W. Zhang, D. Cobden, W. Yao and X. Xu, Magnetic control of valley pseudospin in monolayer WSe_2, *Nat. Phys.*, 2015, **11**, 148–152.
10 D. MacNeill, C. Heikes, K. F. Mak, Z. Anderson, A. Kormanyos, V. Zolyomi, J. Park and D. Ralph, Breaking of valley degeneracy by magnetic field in monolayer $MoSe_2$, *Phys. Rev. Lett.*, 2015, **114**, 037401.
11 D. Zhong, K. Seyler, X. Y. Linpeng, R. Cheng, N. Sivadas, B. Huang, E. Schmidgall, T. Taniguchi, K. Watanabe, M. Mcguire, W. Yao, D. Xiao, K. M. Fu and X. D. Xu, van der Waals engineering of ferromagnetic semiconductor heterostructures for spin and valleytronics, *Sci. Adv.*, 2017, **3**, e1603113.
12 H. S. Zhang, W. J. Yang, Y. H. Ning and X. H. Xu, Abundant valley-polarized states in two-dimensional ferromagnetic van der Waals heterostructures, *Phys. Rev. B*, 2020, **101**, 205404.
13 H. L. Zeng, J. F. Dai, W. Yao, D. Xiao and X. D. Cui, Valley polarization in MoS_2 monolayers by optical pumping, *Nat. Nanotechnol.*, 2012, **7**, 490–493.
14 Y. C. Cheng, Q. Y. Zhang and U. Schwingenschlogl, Valley polarization in magnetically doped single-layer transition-metal dichalcogenides, *Phys. Rev. B: Condens. Matter Mater. Phys.*, 2014, **89**, 155429.
15 N. Singh and U. Schwingenschlogl, A route to permanent valley polarization in monolayer MoS_2, *Adv. Mater.*, 2017, **29**, 1600970.
16 X. Li, T. Cao, Q. Niu, J. R. Shi and J. Feng, Coupling the valley degree of freedom to antiferromagnetic order, *Proc. Natl. Acad. Sci. U. S. A.*, 2013, **110**, 3738–3742.
17 W. Y. Tong, S. J. Gong, X. G. Wan and C. G. Duan, Concepts of ferrovalley material and anomalous valley Hall effect, *Nat. Commun.*, 2016, **7**, 13612.
18 C. M. Zhang, Y. H. Nie, S. Sanvito and A. J. Du, First-principles prediction of a room temperature ferromagnetic Janus VSSe monolayer with piezoelectricity, ferroelasticity, and large valley polarization, *Nano Lett.*, 2019, **19**, 1366–1370.
19 X. D. Zhou, R. W. Zhang, Z. Y. Zhang, W. X. Feng, Y. Mokrousov and Y. G. Yao, Sign-reversible valley-dependent Berry phase effects in 2D valley-half-semiconductors, *npj Comput. Mater.*, 2021, **7**, 160.
20 K. Sheng, Q. Chen, H. K. Yuan and Z. Y. Wang, Monolayer CeI_2: an intrinsic room-temperature ferrovalley semiconductor, *Phys. Rev. B*, 2022, **105**, 075304.

21 K. Jia, X. J. Dong, S. S. Li, W. X. Ji and C. W. Zhang, Spontaneous valley polarization and valley-nonequilibrium quantum anomalous Hall effect in Janus monolayer ScBrI, *Nanoscale*, 2023, **15**, 8395–8405.
22 Z. He, R. Peng, Y. Dai, B. Huang and Y. Ma, Single-layer ScI_2: A paradigm for valley-related multiple Hall effect, *Appl. Phys. Lett.*, 2021, **119**, 243102.
23 P. Jiang, L. Kang, Y. L. Li, X. Zheng, Z. Zeng and S. Sanvito, Prediction of the two-dimensional Janus ferrovalley material LaBrI, *Phys. Rev. B*, 2021, **104**, 035430.
24 Y. M. Zang, Y. D. Ma, R. Peng, H. Wang, B. B. Huang and Y. Dai, Large valley-polarized state in single-layer NbX_2 (X = S, Se): theoretical prediction, *Nano Res.*, 2020, **14**, 834–839.
25 K. Sheng, B. K. Zhang, H. K. Yuan and Z. Y. Wang, Strain-engineered topological phase transitions in ferrovalley 2H-$RuCl_2$ monolayer, *Phys. Rev. B*, 2022, **105**, 195312.
26 R. Li, J. W. Jiang, W. B. Mi and H. L. Bai, Room temperature spontaneous valley polarization in two-dimensional FeClBr monolayer, *Nanoscale*, 2021, **13**, 14807–14813.
27 S. D. Guo, W. Q. Mu and B. G. Liu, Correlation-driven three-fold topological phase transition in monolayer $OsBr_2$, *Front. Phys.*, 2021, **18**, 33304.
28 S. D. Guo, W. Q. Mu and B. G. Liu, Valley-polarized quantum anomalous Hall insulator in monolayer $RuBr_2$, *2D Mater.*, 2022, **9**, 035011.
29 H. Sun, S. S. Li, W. X. Ji and C. W. Zhang, Valley-dependent topological phase transition and quantum anomalous valley Hall effect in single-layer RuClBr, *Phys. Rev. B*, 2022, **105**, 195112.
30 K. Jia, X. J. Dong, S. S. Li, W. X. Ji and C. W. Zhang, Electronic-correlation induced sign-reversible Berry phase and valley-nonequilibrium quantum anomalous Hall effect in the Janus monolayer OsClBr, *Phys. Chem. Chem. Phys.*, 2023, **25**, 15767–15776.
31 K. Jia, X. J. Dong, S. S. Li, W. X. Ji and C. W. Zhang, Strain-engineering induced topological phase transitions and multiple valley states in Janus monolayer $VCSiN_4$, *J. Mater. Chem. C*, 2023, **11**, 10359–10369.
32 W. R. Liu, X. J. Dong, Y. Z. Lv, W. X. Ji, Q. Cao, P. J. Wang, F. Li and C. W. Zhang, Magnetic anisotropy and ferroelectric-driven magnetic phase transition in monolayer $Cr_2Ge_2Te_6$, *Nanoscale*, 2022, **14**, 3632–3643.
33 L. Zhang, S. F. Zhang, W. X. Ji, C. W. Zhang, P. Li, P. J. Wang, S. S. Li and S. S. Yan, Discovery of a novel spin-polarized nodal ring in a two-dimensional HK lattice, *Nanoscale*, 2018, **10**, 20748–20753.
34 S. J. Zhang, C. W. Zhang, S. F. Zhang, W. X. Ji, P. Li, P. J. Wang, S. S. Li and S. S. Yan, Intrinsic Dirac half-metal and quantum anomalous Hall phase in a hexagonal metal-oxide lattice, *Phys. Rev. B*, 2017, **96**, 205433.
35 S. S. Li, W. X. Ji, S. J. Hu, C. W. Zhang and S. S. Yan, Effect of Amidogen Functionalization on Quantum Spin Hall Effect in Bi/Sb(111) Films, *ACS Appl. Mater. Interfaces*, 2017, **9**, 41443–41453.
36 Y. P. Wang, W. X. Ji, C. W. Zhang, P. Li, S. F. Zhang, P. J. Wang, S. S. Li and S. S. Yan, Two-dimensional arsenene oxide: A realistic large-gap quantum spin Hall insulator, *Appl. Phys. Lett.*, 2017, **110**, 213101.
37 M. H. Zhang, C. W. Zhang, P. J. Wang and S. S. Li, Prediction of high-temperature Chern insulator with half-metallic edge states in asymmetry-functionalized stanene, *Nanoscale*, 2018, **10**, 20226–20233.
38 B. Wu, Y. L. Song, W. X. Ji, P. J. Wang, S. F. Zhang and C. W. Zhang, Quantum anomalous Hall effect in an antiferromagnetic monolayer of MoO, *Phys. Rev. B*, 2023, **107**, 214419.
39 Y. T. Han, W. X. Ji, P. J. Wang, P. Li and C. W. Zhang, Strain-tunable skyrmions in two-dimensional monolayer Janus magnets, *Nanoscale*, 2023, **15**, 6830–6837.
40 Y. L. Hong, Z. B. Liu, L. Wang, T. Y. Zhou, W. Ma, C. Xu, S. Feng, L. Chen, M. L. Chen, D. M. Sun, X. Q. Chen, H. M. Cheng and W. C. Ren, Chemical vapor deposition of layered two-dimensional $MoSi_2N_4$ materials, *Science*, 2020, **369**, 670–674.
41 Q. R. Cui, Y. M. Zhu, J. H. Liang, P. Cui and H. X. Yang, Spin-valley coupling in a two-dimensional VSi_2N_4 monolayer, *Phys. Rev. B*, 2021, **103**, 085421.
42 C. Yang, Z. Song, X. Sun and J. Lu, Valley pseudospin in monolayer $MoSi_2N_4$ and $MoSi_2As_4$, *Phys. Rev. B*, 2021, **103**, 035308.
43 J. Huang, P. Li, X. Ren and Z. X. Guo, Promising Properties of a Sub-5 nm Monolayer $MoSi_2N_4$ Transistor, *Phys. Rev. Appl.*, 2021, **16**, 044022.
44 H. Zhong, W. Xiong, P. Lv, J. Yu and S. Yuan, Strain-induced semiconductor to metal transition in MA_2Z_4 bilayers (M = Ti, Cr, Mo; A = Si; Z = N, P), *Phys. Rev. B*, 2021, **103**, 085124.
45 Y. T. Ren, L. Hu, Y. T. Chen, Y. J. Hu, J. L. Wang, P. L. Gong, H. Zhang, L. Huang and X. Q. Shi, Two-dimensional MSi_2N_4 monolayers and van der Waals heterostructures: Promising spintronic properties and band alignments, *Phys. Rev. Mater.*, 2022, **6**, 064006.
46 Y. Yin, Q. H. Gong, M. Yi and W. L. Guo, Emerging Versatile Two-Dimensional $MoSi_2N_4$ Family, *Adv. Funct. Mater.*, 2023, **33**, 2214050.
47 C. C. Tho, S. D. Guo, S. J. Liang, W. L. Ong, C. S. Lau, L. M. Cao, G. Z. Wang and Y. S. Ang, MA_2Z_4 family heterostructures: Promises and prospects, *Appl. Phys. Rev.*, 2023, **10**, 041307.
48 Q. Q. Wang, L. M. Cao, S. J. Liang, W. K. Wu, G. Z. Wang, C. H. Lee, W. L. Ong, H. Y. Yang, L. K. Ang, S. A. Yang and Y. S. Ang, Efficient Ohmic contacts and built-in atomic sublayer protection in $MoSi_2N_4$ and WSi_2N_4 monolayers, *npj 2D Mater. Appl.*, 2021, **5**, 71.
49 C. C. Tho, C. Yu, Q. Tang, Q. Wang, T. Su, Z. Feng, Q. Wu, C. V. Nguyen, W. Ong, S. Liang, S. Guo, L. Cao, S. Zhang, S. A. Yang, L. K. Ang, G. Wang and Y. S. Ang, Cataloguing $MoSi_2N_4$ and WSi_2N_4 van der Waals Heterostructures: An Exceptional Material Platform for Excitonic Solar Cell Applications, *Adv. Mater. Interfaces*, 2023, **10**, 2201856.
50 Z. B. Liu, L. Wang, Y. L. Hong, X. Q. Chen, H. M. Cheng and W. C. Ren, Two-dimensional superconducting

$MoSi_2N_4(MoN)_{4n}$ homologous compounds, *Natl. Sci. Rev.*, 2023, **10**, nwac273.

51 C. C. Tho, X. K. Feng, Z. L. Jiang, L. M. Cao, G. Z. Wang, C. S. Lau, S. D. Guo and Y. S. Ang, Ultrathick MA_2N_4(M′N) Intercalated Monolayers with Sublayer-Protected Fermi Surface Conduction States: Interconnect and Metal Contact Applications, *arXiv*, 2023, preprint, arXiv:2311.09057, DOI: 10.48550/arXiv.2311.09057.

52 A. Y. Lu, H. Zhu, J. Xiao, C. P. Chuu, Y. Han, M. H. Chiu, C. C. Cheng, C. W. Yang, K. H. Wei, Y. Yang, Y. Wang, D. Sokaras, D. Nordlund, P. Yang, D. A. Muller, M. Y. Chou, X. Zhang and L. J. Li, Janus monolayers of transition metal dichalcogenides, *Nat. Nanotechnol.*, 2017, **12**, 744–749.

53 G. Kresse and J. Hafner, Ab initio molecular-dynamics simulation of the liquid-metal-amorphous-semiconductor transition in germanium, *Phys. Rev. B: Condens. Matter Mater. Phys.*, 1994, **49**, 14251.

54 P. E. Blochl, Projector augmented-wave method, *Phys. Rev. B: Condens. Matter Mater. Phys.*, 1994, **50**, 17953.

55 G. Kresse and J. Furthmuller, Efficient iterative schemes for ab initio total-energy calculations using a plane-wave basis set, *Phys. Rev. B: Condens. Matter Mater. Phys.*, 1996, **54**, 11169.

56 J. P. Perdew, K. Burke and M. Ernzerhof, Generalized Gradient Approximation Made Simple, *Phys. Rev. Lett.*, 1996, **77**, 3865.

57 S. L. Dudarev, G. A. Botton, S. Y. Savrasov, C. J. Humphreys and A. P. Sutton, Electron-energy-loss spectra and the structural stability of nickel oxide: An LSDA + U study, *Phys. Rev. B: Condens. Matter Mater. Phys.*, 1998, **57**, 1505.

58 D. Dey, A. Ray and L. P. Yu, Intrinsic ferromagnetism and restrictive thermodynamic stability in MA_2N_4 and Janus $VSiGeN_4$ monolayers, *Phys. Rev. Mater.*, 2022, **6**, L061002.

59 S. D. Guo, W. Q. Mu, J. H. Wang, Y. X. Yang, B. Wang and Y. S. Ang, Strain effects on the topological and valley properties of the Janus monolayer $VSiGeN_4$, *Phys. Rev. B*, 2022, **106**, 064416.

60 A. V. Krukau, O. A. Vydrov, A. F. Izmaylov and G. E. Scuseria, Influence of the exchange screening parameter on the performance of screened hybrid functionals, *J. Chem. Phys.*, 2006, **125**, 224106.

61 X. Wu, D. Vanderbilt and D. R. Hamann, Systematic treatment of displacements, strains, and electric fields in density-functional perturbation theory, *Phys. Rev. B: Condens. Matter Mater. Phys.*, 2005, **72**, 035105.

62 A. Togo, F. Oba and I. Tanaka, First-principles calculations of the ferroelastic transition between rutile-type and $CaCl_2$-type SiO_2 at high pressures, *Phys. Rev. B: Condens. Matter Mater. Phys.*, 2008, **78**, 134106.

63 A. A. Mostofi, J. R. Yates, Y. S. Lee, I. Souza, D. Vanderbilt and N. Marzari, wannier90: A tool for obtaining maximally-localised Wannier functions, *Comput. Phys. Commun.*, 2008, **178**, 685–699.

64 X. Wang, J. R. Yates, I. Souza and D. Vanderbilt, Ab initio calculation of the anomalous Hall conductivity by Wannier interpolation, *Phys. Rev. B: Condens. Matter Mater. Phys.*, 2006, **74**, 195118.

65 L. Wang, Y. Shi, M. Liu, A. Zhang, Y.-L. Hong, R. Li, Q. Gao, M. Chen, W. Ren, H.-M. Cheng, Y. Li and X.-Q. Chen, Intercalated architecture of MA_2Z_4 family layered van der Waals materials with emerging topological, magnetic and superconducting properties, *Nat. Commun.*, 2021, **12**, 2361.

66 V. Vierimaa, A. V. Krasheninnikov and H. P. Komsa, Phosphorene under electron beam: from monolayer to one-dimensional chains, *Nanoscale*, 2016, **8**, 7949–7957.

67 L. M. Yang, I. A. Popov, A. I. Boldyrev, T. Heine, T. Frauenheim and E. Ganz, Post-anti-van't Hoff-Le Bel motif in atomically thin germanium-copper alloy film, *Phys. Chem. Chem. Phys.*, 2015, **17**, 17545–17551.

68 R. C. Andrew, R. E. Mapasha, A. M. Ukpong and N. Chetty, Mechanical properties of graphene and boronitrene, *Phys. Rev. B: Condens. Matter Mater. Phys.*, 2012, **85**, 125428.

69 S. Haastrup, M. Strange, M. Pandey, T. Deilmann, P. S. Schmidt, N. F. Hinsche, M. N. Gjerding, D. Torelli, P. M. Larsen, A. C. Riis-Jensen, J. Gath, K. W. Jacobsen, J. J. Mortensen, T. Olsen and K. S. Thygesen, The Computational 2D Materials Database: high-throughput modeling and discovery of atomically thin crystals, *2D Mater.*, 2018, **5**, 042002.

70 M. Mazdziarz, Comment on 'The Computational 2D Materials Database: high-throughput modeling and discovery of atomically thin crystals', *2D Mater.*, 2019, **6**, 048001.

71 B. Goodenough, Theory of the role of covalence in the Perovskite-type manganites [La, M(II)] MnO_3, *Phys. Rev.*, 1955, **100**, 564.

72 J. Kanamori, Superexchange interaction and symmetry properties of electron orbitals, *J. Phys. Chem. Solids*, 1959, **10**, 87–98.

73 P. W. Anderson, New approach to the theory of superexchange interactions, *Phys. Rev.*, 1959, **115**, 2.

74 G. Benedek and G. F. Nardelli, Evidence for Resonant-Mode Sidebands in Alkali Halides, *Phys. Rev. Lett.*, 1966, **17**, 1136.

75 X. Liu, H. C. Hsu and C. X. Liu, In-Plane Magnetization-Induced Quantum Anomalous Hall Effect, *Phys. Rev. Lett.*, 2013, **111**, 086802.

76 D. J. Thouless, M. Kohmoto, M. P. Nightingale and M. den Nijs, Quantized Hall Conductance in a Two-Dimensional Periodic Potential, *Phys. Rev. Lett.*, 1982, **49**, 405.

77 X. K. Feng, C. S. Lau, S. J. Liang, C. H. Lee, S. A. Yang and Y. S. Ang, Half-Valley Ohmic Contact: Contact-Limited Valley-Contrasting Current Injection, *Adv. Funct. Mater.*, 2023, 2309848.

78 S. D. Guo, X. S. Guo, G. Z. Wang, K. Cheng and Y. S. Ang, Electric-field induced magnetic-anisotropy transformation to achieve spontaneous valley polarization, *J. Mater. Chem. C*, 2022, **10**, 16363–16369.

79 S. D. Guo, Y. L. Tao, H. T. Guo, Z. Y. Zhao, B. Wang, G. Z. Wang and X. T. Wang, Possible electronic state quasi-half-valley metal in a VGe_2P_4 monolayer, *Phys. Rev. B*, 2023, **107**, 054414.